Nanoscale

ROYAL SOCIETY OF CHEMISTRY

PAPER

View Article Online
View Journal | View Issue

Check for updates

Cite this: *Nanoscale*, 2021, **13**, 8181

Plant tissue imaging with bipyramidal upconversion nanocrystals by introducing Tm^{3+} ions as energy trapping centers†

Yufang Qiao,‡[a] Shuqian Qiao,‡[b] Xue Yu,[a] Qiuhong Min,[a] Chaojie Pi,[a] Jianbei Qiu,[a] Hongqing Ma,[c] Jianhong Yi,[a] Qiuqiang Zhan *[b] and Xuhui Xu *[a]

Received 15th October 2020,
Accepted 5th April 2021

DOI: 10.1039/d0nr07399g

rsc.li/nanoscale

Plant cell imaging is critical for agricultural production and plant pathology study. Advanced upconversion nanoparticles (UCNPs) are being developed as fluorescent probes for imaging cells and tissues *in vivo and in vitro*. Unfortunately, the thick cellulosic walls as barriers together with hemicelluloses and pectin hinder the entrance of macromolecules into the epidermal plant cell. Hence, realizing satisfactory temporal and spatial resolution with UCNPs remains an arduous task. Here, bipyramidal $LiErF_4$:1%Tm^{3+}@$LiYF_4$ core–shell UCNPs with a super-bright red emission upon 980 nm laser excitation are explored, where the introduction of Tm^{3+} ions permits alleviation of the energy loss at defective sites and a significant improvement of the upconversion output. The as-obtained bipyramidal UCNPs could readily puncture plant cell walls and further penetrate into cell membranes, facilitating improved tissue imaging of cellular internalization, as demonstrated with the luminescence images obtained by multiphoton laser-scanning microscopy. Hence our work opens up a new avenue for exploring effective upconversion nanoparticles for achieving high resolution imaging of plant tissues.

Published on 07 April 2021. Downloaded on 10/26/2025 3:23:44 PM.

1. Introduction

Fluorescence bioimaging techniques that provide direct information of biospecimens with the features of real-time response and non-invasion have been widely developed in the last decades, and they play an increasingly important role in both fundamental scientific research and clinical practice.[1,2] More recently, an increasing tendency appears to apply nanomaterials as biomarkers for fluorescence bio-imaging *in vivo and in vitro*.[3,4] Lanthanide-doped upconversion nanoparticles (UCNPs) as fluorescent nanoprobes have evoked considerable interest due to their superior features, such as low toxicity, superior photostability, and the elimination of background autofluorescence, which makes them extremely suitable as alternatives, replacing traditional organic fluorescent dyes or quantum dots.[5–11]

To date, UCNPs with surface modification have been widely reported in mammalian cell imaging, but rarely in plant cells due to the challenging properties of plant materials.[12] A typical epidermal plant cell routinely used in microscopic imaging studies comprises a cell wall of considerable thickness, a plasma membrane, a thin layer of cortical cytoplasm with motile organelles, and a vacuole. The most characteristic component of the plant cell wall is cellulose; together with hemicelluloses and pectin, such thick cellulosic barriers impede the passage of macromolecules into the cell.[13,14] According to the previous research, the pore diameter of the plant cell wall ranges from 3 to 10 nm.[15] In fact, UCNPs with a diameter larger than the pore size of plant cell walls hardly penetrate into plant cells.[16] Moreover, the decreased particle size of UCNPs is adverse to the upconversion luminescence output, contributing to the failure of the imaging with satisfactory resolution as well.[17] Hence, the successful uptake and application of UCNPs in plant imaging is still far from satisfactory.

Recently, the morphology of particles has been found to play a crucial role in their uptake in cells, and instituted as a new important parameter for designing materials inducing a specific biological response.[18] Oriented nanomaterials such as nanowires, nanotubes or bullet-shaped nanoparticles have been receiving attention.[19,20] Their elongated shape enables multivalent interactions with receptors through the introduction of multiple targeting units on their surface, thereby

[a]*Faculty of Materials Science and Engineering, Kunming University of Science and Technology, Kunming, 650093, China. E-mail: xuxuh07@126.com*
[b]*Centre for Optical and Electromagnetic Research, South China Academy of Advanced Optoelectronics, South China Normal University, Guangzhou, 510006, China. E-mail: zhanqiuqiang@m.scnu.edu.cn*
[c]*Shandong Provincial Key Laboratory of Soil Conservation and Environmental Protection, College of Resources and Environment, Linyi University, Linyi, 276000, China*

†Electronic supplementary information (ESI) available. See DOI: 10.1039/d0nr07399g

‡These authors contributed equally.

Published on 07 April 2021. Downloaded on 10/26/2025 3:23:44 PM.

enhancing cell internalization.[21,22] For example, McCarthy and co-workers demonstrated that the cellular uptake of magnetic-fluorescent nanowires depends on their aspect ratio.[23] Chen's group reported that hexagonal bipyramid quantum dots could readily "puncture" into the lipid bilayer and break the integrity of the cell membrane when attached on the cell surface with the apex.[24] These results inspire us to explore oriented UCNPs that readily penetrate plant cells and possess high sensitivity and signal-to-noise ratio to meet the requirement of fluorescent probe imaging of plants and tissue.

In this work, Tm^{3+} ion doped bipyramidal $LiErF_4$@$LiYF_4$ core–shell UCNPs with high red upconversion luminescence were synthesized by a co-precipitation method.[25] We demonstrated the feasibility of enhancing the red emission of the Er^{3+}-enriched $LiErF_4$ UCNPs by coating with a bipyramidal shell, while the introduction of Tm^{3+} ions acting as energy trapping centers could further optimize the upconversion performance. The red light falls into the optical transmittance window of biological tissues and provides deep tissue penetration. Plant cell imaging is demonstrated by labeling onion epidermal cells with the as-synthesized $LiErF_4$:1%Tm^{3+}@$LiYF_4$ UCNPs. Compared with the spherical counterparts, the bipyramidal $LiErF_4$@$LiYF_4$ core–shell UCNPs with a higher aspect ratio are shown to penetrate into cell walls and break cell membranes, giving significantly improved cellular internalization for imaging, which is captured with multiphoton laser-scanning luminescence images. These results demonstrate that bipyramidal UCNPs are particularly attractive for intracellular labeling and imaging of plants and tissue.

2. Results and discussion

$LiErF_4$ UCNPs doped with Tm^{3+} ions with the concentration varying from 0 to 20 at% were synthesized by a co-precipitation method[26] (Fig. S1, ESI†). The optimal doping concentration of Tm^{3+} ions for $LiErF_4$ is determined to be 1% for the maximum upconversion luminescence intensity output (Fig. S2, ESI†). The as-obtained $LiErF_4$:1%Tm^{3+} UCNPs exhibit a regular and uniform morphology with a mean particle size of 8 nm as displayed in Fig. 1a and c. After coating with an inert $LiYF_4$ shell, an identical crystal structure of the $LiErF_4$:1%Tm^{3+}@$LiYF_4$ is

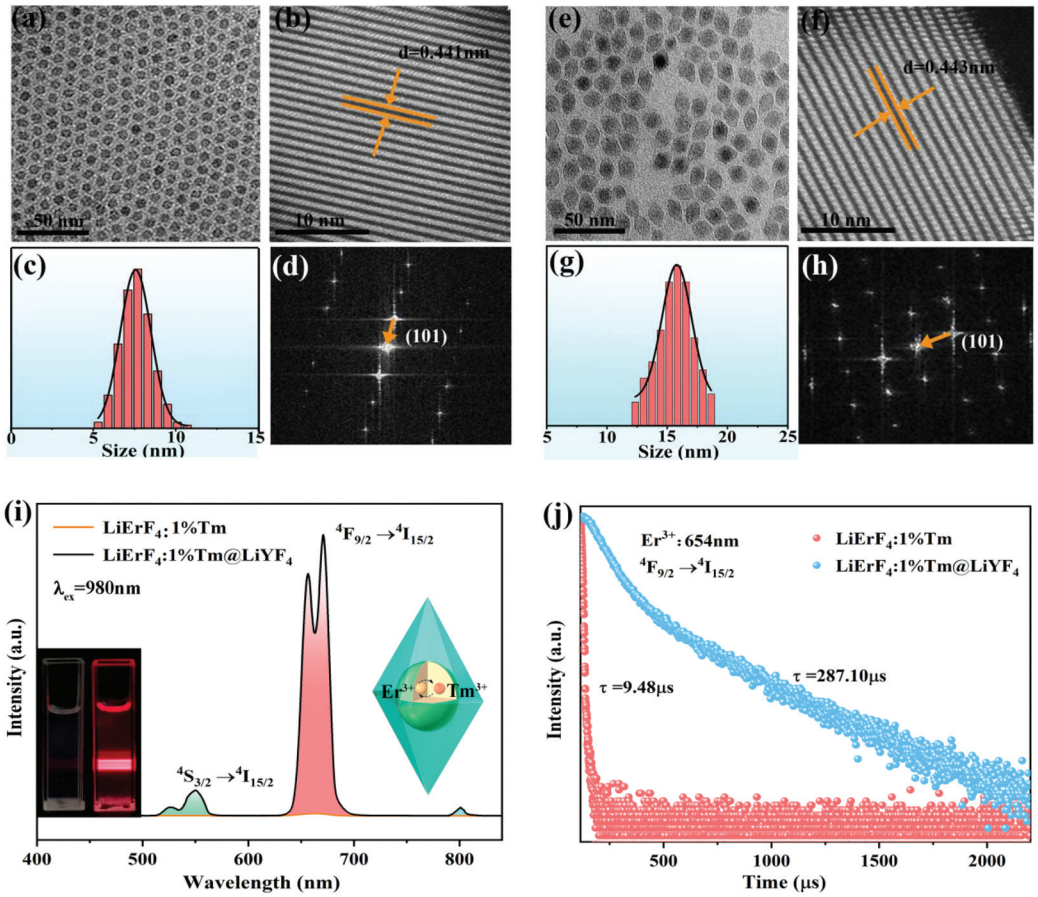

Fig. 1 TEM images, HRTEM images, particle size distribution, and the corresponding FFT of $LiErF_4$:1%Tm^{3+} (a–d) and $LiErF_4$:1%Tm^{3+}@$LiYF_4$ (e–h) UCNPs, respectively. (i) Upconversion emission spectra of $LiErF_4$:1%Tm^{3+} and $LiErF_4$:1%Tm^{3+}@$LiYF_4$ UCNPs under 980 nm excitation, the left inset shows the photographs of the corresponding samples under 980 nm excitation, and the right inset is the schematic illustration of the $LiErF_4$:1% Tm^{3+}@$LiYF_4$ core–shell structure. (j) The corresponding decay curves of Er^{3+} ions (654 nm) of $LiErF_4$:1%Tm^{3+} and $LiErF_4$:1%Tm^{3+}@$LiYF_4$ UCNPs under 980 nm excitation.

 This journal is © The Royal Society of Chemistry 2021

Published on 07 April 2021. Downloaded on 10/26/2025 3:23:44 PM.

confirmed from the XRD patterns (Fig. S3, ESI†), and no trace of other phases or impurities is detected. The energy dispersive spectroscopy image (Fig. S4, ESI†) demonstrates the existence of the elements of Er, Y, and Tm in the nanocrystal. Moreover, the image of the $LiErF_4$:1%Tm^{3+}@$LiYF_4$ UCNPs in the dark field is further provided in the inset of Fig. S4,† which confirms the as-prepared $LiErF_4$:1%Tm^{3+}@$LiYF_4$ UCNPs with a bipyramidal structure. The low-resolution transmission electron microscopy (TEM) image of $LiErF_4$:1%Tm^{3+}@$LiYF_4$ core–shell UCNPs shown in Fig. 1e presents a bipyramidal shape morphologically. Physical dimensions of the $LiErF_4$:1% Tm^{3+}@$LiYF_4$ core–shell UCNPs are obtained factoring minor × major axis of an elliptical fit for individual bipyramidal UCNPs (Fig. 1g and Fig. S5, ESI†), and are estimated to be 10 × 15 nm. Consistent results of the high resolution transmission electron microscopy (HRTEM) image and the corresponding fast Fourier transform (FFT) diffraction patterns of the $LiErF_4$ (Fig. 1b and d) and $LiErF_4$:1%Tm^{3+}@$LiYF_4$ (Fig. 1f and h) are displayed, respectively, which shows a highly crystalline tetragonal phase of the as-synthesized nanocrystals. Under 980 nm laser excitation, two primary upconversion emission peaks of Er^{3+} ions located at 545 ($^4S_{3/2} \rightarrow {}^4I_{15/2}$) and 654 nm ($^4F_{9/2} \rightarrow {}^4I_{15/2}$) are observed (Fig. 1i), respectively. Significantly, after the nuclear $LiErF_4$:1%Tm^{3+} UCNPs are grown with an inert shell of $LiYF_4$, the upconversion luminescence intensity of 654 nm increases by about 562 times as illustrated in Fig. 1i and displayed as the inset photographs of Fig. 1i. Moreover, the decay curves recorded at the emission of 654 nm of $LiErF_4$:1%Tm^{3+} and $LiErF_4$:1%Tm^{3+}@$LiYF_4$ UCNPs are well-fitted with the double-exponential decay mode, as depicted in Fig. 1j, respectively. The decay time of Er^{3+} ions significantly increases from 9.48 to 287.10 μs after coating with an inert shell. It infers the superiority of the core–shell structure, which suppresses the luminescence quenching caused by the energy migration to surface defects.[27,28]

A series of $LiYF_4$:x%Er^{3+} UCNPs were synthesized (Fig. S6 and S7, ESI†). The visible green ($^4S_{3/2} \rightarrow {}^4I_{15/2}$) and red ($^4F_{9/2} \rightarrow {}^4I_{15/2}$) emission intensity decreases with the increasing Er^{3+} ion concentration, while it is almost completely quenched for 100 mol% Er^{3+} doping (Fig. S8, ESI†). The concentration quenching is suggested due to the cross-relaxation quenching between Er^{3+} ions in close proximity, and the energy transfer to the defects.[29,30] In contrast, the luminescence intensity of the $LiErF_4$ coating with a $LiYF_4$ shell increases monotonically with the increased Er^{3+} ion concentration (Fig. 2a, S10 and S11, ESI†), suggesting that the concentration quenching effect of the red emission can be effectively minimized by coating with an epitaxial shell. Moreover, the red/green (R/G) ratio of these samples changes from 1.5 to 9.3, achieving the upconversion output colour changes from green to red, which is confirmed by the inset photographs of Fig. 2a. Moreover, the time-resolved population properties of the red emission of Er^{3+} ions ($^4F_{9/2}$) of $LiYF_4$:Er^{3+} and $LiYF_4$:Er^{3+}@$LiYF_4$ UCNPs were recorded upon 980 nm laser excitation, respectively (Fig. S9 and S12, ESI†). The lifetime of the $^4F_{9/2}$ state decreases from 112.5 to 12.36 μs along with the increase of the concentration of Er^{3+} ions for the $LiYF_4$:Er^{3+} sample, which is consistent with the above photoluminescence results for the increased probability of energy migrating to the surface defects and the interionic distance shortens as the Er^{3+} ion concentration increases.[31] On the contrary, $LiYF_4$:Er^{3+}@$LiYF_4$ UCNPs exhibit much longer luminescence lifetimes changing from 584.52 to 395.23 μs when the concentration of Er^{3+} ions increases. This demonstrates that even under high dopant concentrations that in principle favor rapid cross relaxation, no concentration quenching is observed in the lifetime or the emission intensity of $LiYF_4$:Er^{3+}@$LiYF_4$ UCNPs. This suggests that energy migration to surface defects is the dominant mechanism for concentration quenching in the nanocrystals heavily doped with Er^{3+} ions, rather than the cross relaxation.[32]

It should be pointed out that Tm^{3+} ions play a critical role in further enhancing the red emission of the Er^{3+}-based host matrix (Fig. 2a). The surface coating method is scarcely mitigated the concentration quenching caused by the energy migration to internal defects,[33] it is strongly demonstrated that Tm^{3+} ions as energy trapping centers alleviate the energy loss at internal defect sites and allow for energy return to Er^{3+} activators.[34] Although the doped Tm^{3+} ions favor luminescence intensity, we noticed that with the increasing Tm^{3+} content over 1%, the intense cross-relaxation (Tm^{3+}–Tm^{3+}) effect inevitably results in fluorescence quenching (Fig. S13 and S14, ESI†).[35,36] The mechanism of $LiErF_4$:1%Tm^{3+}@$LiYF_4$ UCNPs upon 980 nm excitation is shown in Fig. 2c. The electron $^4I_{11/2}$ (Er^{3+} ions) state is populated from $^4I_{15/2}$ by direct absorption of a 980 nm photon or through energy transfer from adjacent Er^{3+} ions. The $^3H_5$ level of Tm^{3+} ions is slightly lower than the $^4I_{11/2}$ level of Er^{3+} ions, which facilitates the energy transfer between Er^{3+} and Tm^{3+} ions ($^4I_{11/2}$ (Er^{3+}) → $^3H_5$ (Tm^{3+})). Then, a back-energy-transfer process occurred between the $^3H_5$ state and the $^4I_{13/2}$ state ($^3H_5$ (Tm^{3+}) → $^4I_{13/2}$ (Er^{3+})), followed by energy pumping with a second 980 nm photon to the $^4F_{9/2}$ state of Er^{3+}, leading to a conspicuous enhancement in red emission at 654 nm.

The laser power (P) dependent properties of the emission intensity (I) of $LiErF_4$:1%Tm^{3+} UCNPs are analyzed as shown in Fig. 2b. The relationship between I and P can be expressed as $I \propto P^n$, where n is the number of pump photons required to populate the excited state.[37] The addition of Tm^{3+} ions to the $LiErF_4$ lattice leads to an obvious decrease in the number of photon processes, especially in the two-photon process for red emission (Fig. S15, ESI†). This is mainly attributed to the efficient energy back transfer process from $^3H_5$ (Tm^{3+}) as the trapping centers to the $^4I_{13/2}$ state of Er^{3+} ions. As a result, assisted by the Tm^{3+} ($^3H_5$) energy trapping center, more photons can be populated into the $^4F_{9/2}$ state of Er^{3+} ions. Meanwhile, the decay lifetime of Er^{3+} ion emission at the $^4F_{9/2}$ state decreases from 395.23 ($LiErF_4$@$LiYF_4$ UCNPs) to 287.10 μs ($LiErF_4$:1%Tm^{3+}@$LiYF_4$ UCNPs) (Fig. S11, ESI†), suggesting that the Tm^{3+} doping causes an increased rate of energy radiations from the $^4F_{9/2}$ state to the $^4I_{15/2}$ state. It should be noted that the three-photon population process for green emission is strongly suppressed, because the distance between Er^{3+} ions shortens with increasing the Er^{3+} ion concentration. This can also lead to an increased rate of

Published on 07 April 2021. Downloaded on 10/26/2025 3:23:44 PM.

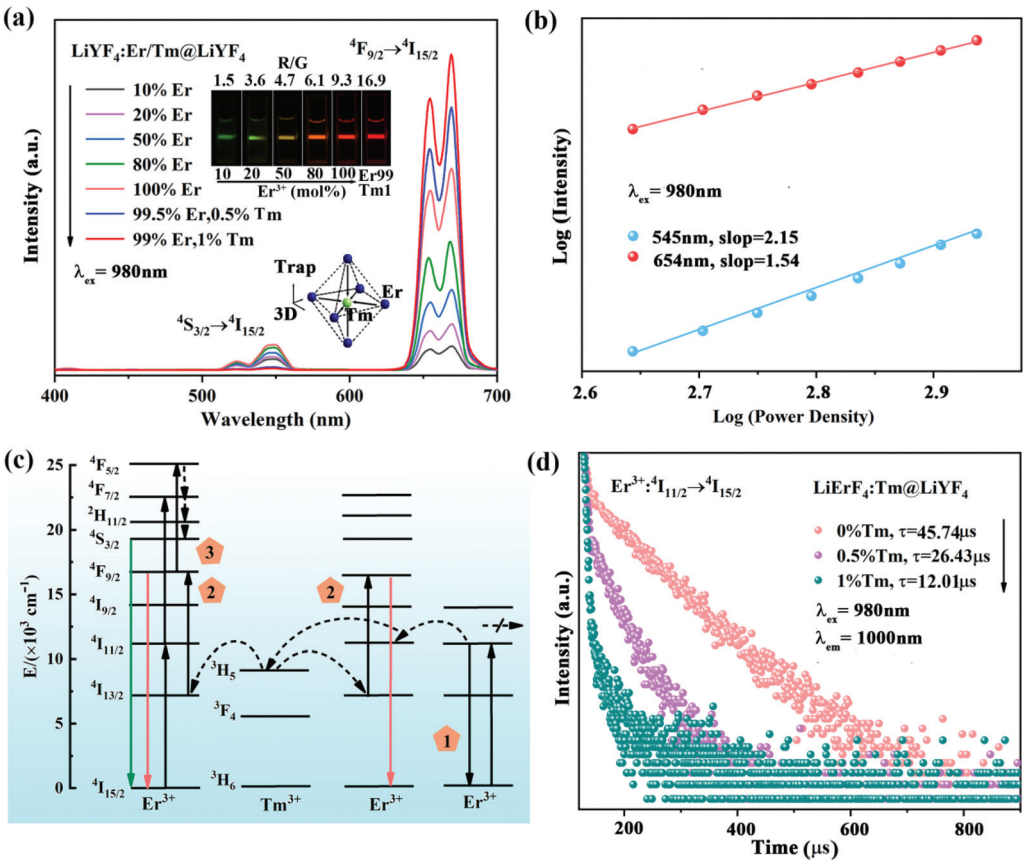

Fig. 2 (a) Upconversion spectra of the as-obtained $LiYF_4:Er^{3+}/Tm^{3+}@LiYF_4$ nanoparticles doped with different concentrations of Er^{3+} and Tm^{3+}. Inset: the photographs of the colloidal dispersion of the corresponding samples under excitation with a 980 nm laser diode, and a structural model for Tm^{3+}-mediated energy condensation between Er^{3+} ions. (b) Power density dependence of the 545 and 654 nm emission, indicating a two-photon population process for the red emission and a three-photon population process for the green emission in the $LiErF_4:1\%Tm^{3+}@LiYF_4$ nanocrystals under 980 nm excitation. (c) Proposed upconversion mechanism for $LiErF_4:1\%Tm^{3+}$ nanoparticles. (d) The luminescence decay curves of Er^{3+} of $LiYF_4:Tm^{3+}@LiYF_4$ with different Tm^{3+} concentrations.

energy migration as confirmed by lifetime measurements of Er^{3+} emission at its $^4F_{9/2}$ state (Fig. S12, ESI†). The time-resolved population at the $^4I_{11/2}$ state of Er^{3+} is investigated as exhibited in Fig. 2d, which implies that the depopulation at the $^4I_{11/2}$ state of Er^{3+} is accelerated by Tm^{3+}-mediated trapping through energy transfer.

Herein, a model is proposed to illustrate the enhancement of the upconversion output. Indeed, the efficiency of $LiErF_4$ UCNPs is limited for the concentration quenching, which can be attributed to the energy migration to surface defects or internal quenching sites (Fig. 3a). Bipyramidal $LiYF_4$ as a coating shell is beneficial to suppress the energy migration loss from Er^{3+} to surface defects, allowing a heavy dopant concentration in $LiErF_4@LiYF_4$ UCNPs (Fig. 3b). Furthermore, Tm^{3+} ions act as energy trapping centers for confining the excitation energy and minimize the migration mediated energy loss in the lattice (Fig. 3c). Hence, further optimized red upconversion emission could be obtained in the $LiYF_4:Tm^{3+}@LiYF_4$ UCNPs.

In order to confirm the feasibility of the as-obtained UCNPs acting as bio-probes, imaging was conducted on onion epidermal cells. After removing oleic acid from the surface of the nanoparticles (treated with hydrochloric acid solution), an aqueous dispersion of $LiErF_4:1\%Tm^{3+}@LiYF_4$ core–shell UCNPs was added into a container with onion epidermal tissues. Before analysis, onion epidermal tissue was cleaned thoroughly with deionized water. The digital photographs of The Onion epidermal tissue with UCNPs are shown in Fig. 4a and b. It can be seen clearly in Fig. 4b that The Onion epidermal cells exhibit naked-eye red upconversion luminescence under irradiation at 980 nm, which indicates the high biocompatibility of $LiErF_4:1\%Tm^{3+}@LiYF_4$ core–shell UCNPs. Moreover, the fluorescence imaging of The Onion epidermal cells with spherical $NaGdF_4:Yb^{3+},Er^{3+}$ UCNPs (as a reference sample, Fig. 4f and S16–S18, ESI†) and bipyramidal $LiErF_4:1\%Tm@LiYF_4$ UCNPs that underwent the same ligand exchange reaction was performed. After removing oleic acid from the surface of the nanoparticles, the two samples with the same concentration are incubated with two onion tissues for 30 min at 25 °C. It can be observed that the red fluorescent nanoparticles penetrate into the cytoplasm (Fig. 4c–e), while the green fluorescent nanoparticles distribute relatively infre-

 This journal is © The Royal Society of Chemistry 2021

Published on 07 April 2021. Downloaded on 10/26/2025 3:23:44 PM.

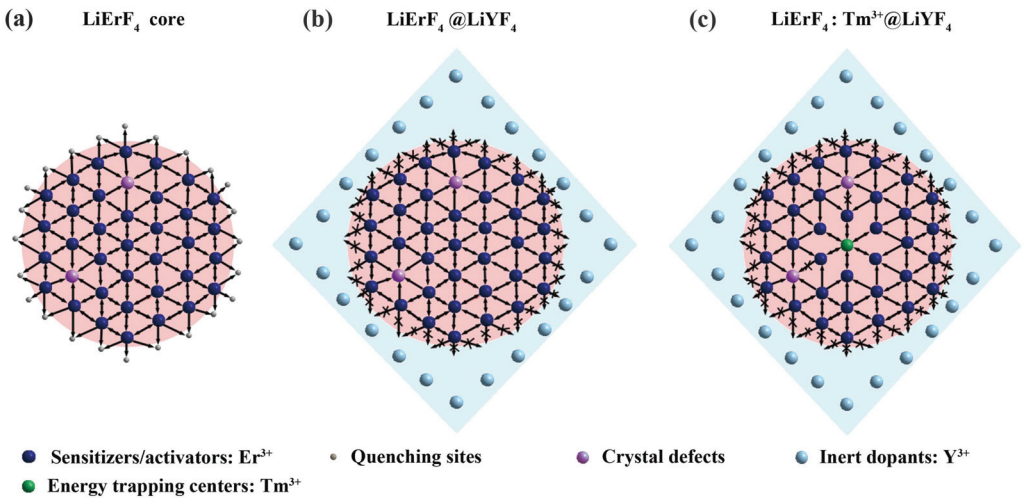

Fig. 3 (a) The energy migration quenching processes in a $LiErF_4$ UCNP. (b) A typical strategy to reduce the energy migration to surface quenching sites through an inert-shell coating. (c) The approach of simultaneously preventing energy migration quenching processes through introducing Tm^{3+} ions as energy trapping centers.

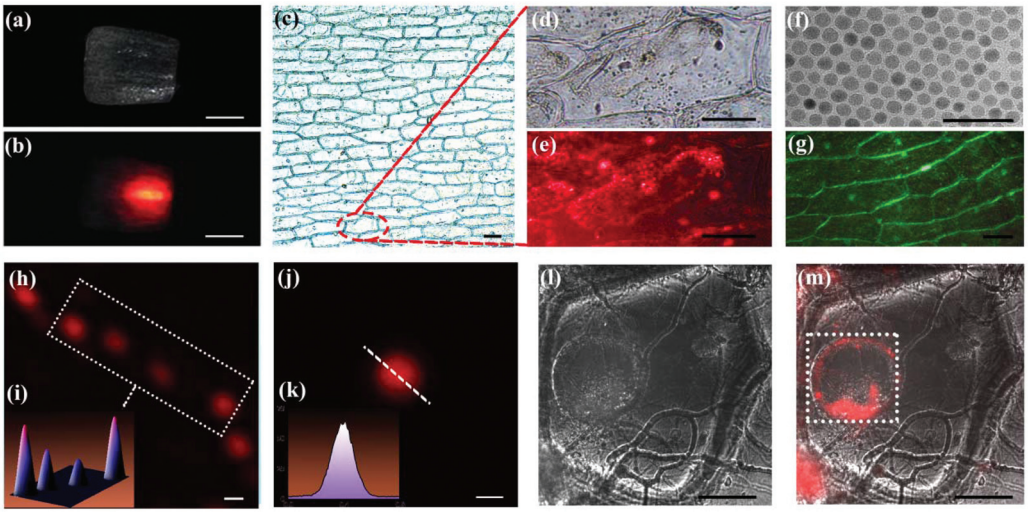

Fig. 4 (a and b) Macroscopic images (scale bar is 5 mm) of onion tissue immersed in $LiErF_4$:1%Tm^{3+}@$LiYF_4$ core–shell UCNP solution with a concentration of 0.2 mg ml^{-1} before and after irradiation with a 980 nm laser. (c) Microscope image of onion epidermal cells after incubation with $LiErF_4$:1%Tm^{3+}@$LiYF_4$ core–shell UCNPs (scale bar is 10 μm). (d and e) Magnified areas selected from Fig. 4c; scale bar is 5 μm. (f) TEM of $NaGdF_4$:Yb^{3+},Er^{3+} core UCNPs; the scale bar in Fig. 4f is 50 nm. (g) Microscope image of onion epidermal cells after incubation with $NaGdF_4$:Yb^{3+},Er^{3+} core UCNP solution with a concentration of 0.2 mg ml^{-1}; the scale bar in Fig. 4g is 8 μm. (h and i) The super-resolution images and the corresponding three-dimensional representation of single a $LiErF_4$:1%Tm^{3+}@$LiYF_4$ core–shell UCNP; the scale bar in Fig. 4h is 1 μm. (j and k) Image from Fig. 4h and the corresponding line profiles of the image; the scale bar in Fig. 4j is 1 μm. (l and m) The confocal luminescence images of onion epidermal cells after incubation with $LiErF_4$:1%Tm^{3+}@$LiYF_4$ core–shell UCNPs before and after irradiation with a 980 nm laser; the scale bars in Fig. 4l and m are 10 μm. All images are obtained under the same exposure conditions.

quently in the cytoplasm, mainly in cell walls (Fig. 4g and S19†).

The optical performance of a single $LiErF_4$:1%Tm^{3+}@$LiYF_4$ core–shell UCNP was recorded *via* multiphoton scanning microscopy, under 980 nm laser light irradiation. Fig. 4h and i exhibit the image and the corresponding three-dimensional representation of $LiErF_4$:1%Tm^{3+}@$LiYF_4$ core–shell UCNPs under a quite low emission density (10 MW cm^{-2}), which means a high signal-to-noise ratio in upconversion luminescence detection. The line profile analysis for a single nanoparticle indicates that the $LiErF_4$:1%Tm^{3+}@$LiYF_4$ core–shell UCNP presents a Gaussian distribution, and the maximum pixel value for the Gaussian spot was used to represent the brightness of these particles, as shown Fig. 4j and k. The result shows that the individual particle in $LiErF_4$:1% Tm^{3+}@$LiYF_4$ core–shell UCNPs can be clearly identified from

Published on 07 April 2021. Downloaded on 10/26/2025 3:23:44 PM.

the particle group, which reveals a high signal-to-noise ratio of $LiErF_4$:1%Tm^{3+}@$LiYF_4$ UCNPs. The multiphoton scanning luminescence images of onion epidermal cells with UCNPs are displayed in Fig. 4l and m. The images visually reveal that the luminescence signals of the $LiErF_4$:1%Tm^{3+}@$LiYF_4$ core–shell UCNPs were mainly located in the nucleus of onion cells.

3. Conclusion

In summary, we have designed bipyramidal $LiErF_4$:1% Tm^{3+}@$LiYF_4$ core–shell UCNPs as fluorescent nanoprobes for onion cell imaging. The resultant bipyramidal $LiErF_4$:1% Tm^{3+}@$LiYF_4$ core–shell UCNPs exhibit high morphological uniformity and generate red emission under 980 nm excitation. The as-explored bipyramidal UCNPs can readily penetrate the plant cell wall and puncture into the cell membrane when attached on the cell surface with the apex. Furthermore, the Tm^{3+}-mediated energy trapping center together with the bipyramidal shell results in a 562-fold luminescence enhancement in Er^{3+}-based host UCNPs, which ensures a high signal-to-noise ratio for optical imaging. The measured fluorescence images indicate that these fluorescent UCNP nanoprobes provide clearly the cell microstructure details. The study of bipyramidal UCNPs paves the way for the development of plant gene labeling technology, which will be beneficial to the monitoring and evaluation of crop species for plant ecology. This work not only provides a convenient platform for the investigation of morphology-dependent properties for cellular uptake, but also offers the possibility of applying UCNPs with specific morphologies for imaging in plant systems.

4. Methods/experimental

Materials

Analytical grade ammonium fluoride (NH_4F, 98%), lithium hydroxide (LiOH, 96%), sodium hydroxide (NaOH, 96%), oleic acid (OA), and 1-octadecene (ODE) were purchased from Aladdin Reagents (Shanghai, China). High purity (99.99%) Tm_2O_3, Y_2O_3, Er_2O_3, Yb_2O_3, and Gd_2O_3 were purchased from Aladdin Reagents (Shanghai, China). All the chemical reagents mentioned above were used directly without further purification. The $RECl_3$ (RE = Y^{3+}, Er^{3+}, Tm^{3+}, and Gd^{3+}) compounds were prepared by dissolving the corresponding RE_2O_3 compounds in a hot HCl solution.

Synthesis of $LiREF_4$:X%Tm^{3+} core nanocrystals (RE = Y^{3+} and Er^{3+})

The $LiYF_4$:x%Er^{3+} (x = 10, 20, 50, 80, and 100) and $LiErF_4$:x% Tm^{3+} (x = 0, 0.5, 1, 5, 10, and 20) UCNPs were prepared by the co-precipitation method. In the typical synthesis, calculated amounts of YCl_3, $ErCl_3$, and $TmCl_3$ to a total of 1 mmol were added into added to a 100 mL three-necked flask containing OA (8 mL) and ODE (12 mL). Then, the mixture was heated to 150 °C for 1 h with vigorous stirring to remove deionized water. After cooling down to room temperature, the LiOH and NH_4F dissolved in methanol (10 mL) were quickly injected into the solution. The mixture was heated at 50 °C for 30 min and then heated at 80 °C for 1 h to remove the methanol. Subsequently, the solution was heated at 280 °C and kept for 90 min under an argon atmosphere. Then the reaction was cooled to room temperature. The UCNPs were collected by centrifugation, washed several times with ethanol, and dispersed in cyclohexane.

Synthesis of $LiREF_4$:X%Tm^{3+}@$LiYF_4$ core–shell UCNPs

$LiYF_4$:x%Er^{3+}@$LiYF_4$ and $LiErF_4$:x%Tm^{3+}@$LiYF_4$ core–shell UCNPs were prepared with an identical procedure as described above. In the typical synthesis, the pre-synthesized core nanoparticles were used as the template for epitaxial growth of the shell layer *via* a two-step reaction.

Synthesis of $NaGdF_4$:Yb^{3+},Er^{3+} core UCNPs

$NaGdF_4$:Yb^{3+},Er^{3+} core UCNPs were prepared with an identical procedure as described above.

General characterization

The power X-ray diffraction (XRD) patterns were recorded on a D8 Focus diffractometer using Cu-Kα radiation (λ = 0.15405 nm) to identify the crystallization phase. The particle size, shape and microstructures were studied with field transmission electron microscopy (TEM) using a JEM-2100 at 200 kV and high-resolution field transmission electron microscopy (HRTEM) using a U.S. FEI TecnaiG2F20 operating at 300 kV. The absorption and emission spectra under 980 nm excitation of the samples were measured using a U4100 spectrometer and a FLAME-S-XR1-ES spectrophotometer (Shenzhen Yanyou Instrument Ltd, Shenzhen, China), respectively. Images were acquired digitally on a NIKON D7100 camera. The decay curves were measured on an Edinburgh FLS980 spectrophotometer. The effective luminescence decay time was calculated by

$$I = A_1 \exp\left(-\frac{t}{\tau_1}\right) + A_2 \exp\left(-\frac{t}{\tau_2}\right) \quad (1)$$

where I is the luminescence intensity, A_1 and A_2 are fitting parameters, t is the time, and τ_1 and τ_2 are the luminescence lifetimes. Based on (1), the average luminescence lifetime τ of 980 nm emission can be calculated by the following equation:

$$\tau = (A_1{\tau_1}^2 + A_2{\tau_2}^2)/(A_1\tau_1 + A_2\tau_2) \quad (2)$$

Plant tissue optical imaging

The onion epidermal slices were dried at a temperature of 25 °C for one day. The UCNPs were washed with 1 ml ethanol and 1 ml hydrochloric acid solution, centrifuged, and then rinsed with 1 ml ethanol and 1 ml aqueous solution twice, and finally water was added for dispersion. An aqueous dispersion of $LiErF_4$:1%Tm^{3+}@$LiYF_4$ core–shell UCNPs was added to a container with onion epidermal slices, which were incubated for 30 min at 25 °C. Imaging of the nanoparticle uptake by

 This journal is © The Royal Society of Chemistry 2021

Published on 07 April 2021. Downloaded on 10/26/2025 3:23:44 PM.

onion epidermal cells was carried out using an Olympus IX81 multiphoton laser-scanning microscope under excitation with a 980 nm NIR laser. All studies were carried out at room temperature.

Conflicts of interest

The authors declare no conflict of interest.

Acknowledgements

This work was financially supported by the Excellent Youth Project of Yunnan Province Applied Basic Research Project (2019FI001), the Yunnan Ten Thousand Talents Plan Young & Elite Talents Project (YNWR-QNBJ-2018-295), the Science and Technology Program of Guangzhou (2019050001), the foundation of Yunnan Province (2019HC016), and Rare and Precious Metal Materials Genome Engineering Project of Yunnan Province (202002AB080001).

References

1 G. Hong, A. L. Antaris and H. Dai, *Nat. Biomed. Eng.*, 2017, **1**, 1–22.
2 R. Weissleder, *Science*, 2006, **312**, 1168–1171.
3 S. Han, A. Samanta, X. Xie, L. Huang, J. Peng, S. J. Park, D. B. L. Teh, Y. Choi, Y.-T. Chang, A. H. All, B. Xing and X. Liu, *Adv. Mater.*, 2017, **29**, 1700244.
4 S. Chinnathambi and N. Shirahata, *Sci. Technol. Adv. Mater.*, 2019, **20**, 337–355.
5 Y. Wang, K. Zheng, S. Song, D. Fan, H. Zhang and X. Liu, *Chem. Soc. Rev.*, 2018, **47**, 6473–6485.
6 A. Zebibula, N. Alifu, L. Xia, C. Sun, X. Yu, D. Xue, L. Liu, G. Li and J. Qian, *Adv. Funct. Mater.*, 2018, **28**, 1703451.
7 M. De, S. Rana, H. Akpinar, O. R. Miranda, R. R. Arvizo, U. H. Bunz and V. M. Rotello, *Nat. Chem.*, 2009, **1**, 461–465.
8 G. Shan, R. Weissleder and S. A. Hilderbrand, *Theranostics*, 2013, **3**, 267.
9 A. P. Alivisatos, W. Gu and C. Larabell, *Annu. Rev. Biomed. Eng.*, 2005, **7**, 55–76.
10 Z. Ma, M. Zhang, J. Yue, C. Alcazar, Y. Zhong, T. C. Doyle, H. Dai and N. F. Huang, *Adv. Funct. Mater.*, 2018, **28**, 1803417.
11 Q. Zhan, H. Liu, B. Wang, Q. Wu, R. Pu, C. Zhou, B. Huang, X. Peng, H. Ågren and S. He, *Nat. Commun.*, 2017, **8**, 1–11.
12 W. Li, Y. Zheng, H. Zhang, Z. Liu, W. Su, S. Chen, Y. Liu, J. Zhuang and B. Lei, *ACS Appl. Mater. Interfaces*, 2016, **8**, 19939–19945.
13 T. R. Mota, D. Oliveira, R. Marchiosi, O. Ferrarese-Filho and W. Santos, *AIMS Bioeng.*, 2018, **5**, 63.
14 N. Gigli-Bisceglia, T. Engelsdorf and T. Hamann, *Cell. Mol. Life Sci.*, 2020, **77**, 2049–2077.
15 Y. Jiang, M. Lawrence, M. Ansell and A. Hussain, *R. Soc. Open Sci.*, 2018, **5**, 171945.
16 Y. Zheng, H. Zhang, W. Li, Y. Liu, X. Zhang, H. Liu and B. Lei, *RSC Adv.*, 2017, **7**, 33459–33465.
17 G. Hong, J. C. Lee, J. T. Robinson, U. Raaz, L. Xie, N. F. Huang, J. P. Cooke and H. Dai, *Nat. Med.*, 2012, **18**, 1841–1846.
18 X. Huang, X. Teng, D. Chen, F. Tang and J. He, *Biomaterials*, 2010, **31**, 438–448.
19 Z. Liu, W. Cai, L. He, N. Nakayama, K. Chen, X. Sun, X. Chen and H. Dai, *Nat. Nanotechnol.*, 2007, **2**, 47–52.
20 E. Bladt, R. J. van Dijk-Moes, J. Peters, F. Montanarella, C. de Mello Donega, D. Vanmaekelbergh and S. Bals, *J. Am. Chem. Soc.*, 2016, **138**, 14288–14293.
21 J. H. Park, G. von Maltzahn, L. Zhang, M. P. Schwartz, E. Ruoslahti, S. N. Bhatia and M. J. Sailor, *Adv. Mater.*, 2008, **20**, 1630–1635.
22 J. H. Park, G. von Maltzahn, L. Zhang, A. M. Derfus, D. Simberg, T. J. Harris, E. Ruoslahti, S. N. Bhatia and M. J. Sailor, *Small*, 2009, **5**, 694–700.
23 J. E. McCarthy, A. Prina-Mello, T. Rakovich, Y. Volkov and Y. K. Gun'ko, *J. Mater. Chem.*, 2011, **21**, 14219–14225.
24 R. Tan, Y. Yuan, Y. Nagaoka, D. Eggert, X. Wang, S. Thota, P. Guo, H. Yang, J. Zhao and O. Chen, *Chem. Mater.*, 2017, **29**, 4097–4108.
25 C. Zhang, P. Zhou, Y. Liao, W. Feng, W. Sun, X. Li, H. Xu, J. Fang, D. Sun, W. Zhang and H. Yan, *Adv. Mater.*, 2010, **22**, 633–637.
26 C. Zhang, P. Zhou, Y. Liao, W. Feng, W. Sun, X. Li, H. Xu, J. Fang, D. Sun, W. Zhang and H. Yan, *Adv. Mater.*, 2010, **22**, 633–637.
27 W. Shao, G. Chen, A. Kuzmin, H. L. Kutscher, A. Pliss, T. Y. Ohulchanskyy and P. N. Prased, *J. Am. Chem. Soc.*, 2016, **138**, 16192–16195.
28 G. Chen, H. Ågren, T. Y. Ohulchanskyy and P. N. Prased, *Chem. Soc. Rev.*, 2015, **44**, 1680–1713.
29 L. Tu, X. Liu, F. Wu and H. Zhang, *Chem. Soc. Rev.*, 2015, **44**, 1331–1345.
30 N. J. J. Johnson, S. He, S. Diao, E. M. Chan, H. Dai and A. Almutairi, *J. Am. Chem. Soc.*, 2017, **139**, 3275–3282.
31 J. W. Stouwdam and F. C. van Veggel, *Nano Lett.*, 2002, **2**, 733–737.
32 Q. Chen, X. Xie, B. Huang, L. Liang, S. Han, Z. Yi, Y. Wang, Y. Li, D. Fan and L. Huang, *Angew. Chem.*, 2017, **129**, 7713–7717.
33 J. Xu, D. Yang, W. Han, S. Dong, T. Jia, F. He, H. Bi, S. Gai, L. Li and P. Yang, *J. Mater. Chem. C*, 2018, **6**, 7533–7540.
34 Y. Shang, S. Hao, W. Lv, T. Chen, L. Tian, Z. Lei and C. Yang, *J. Mater. Chem. C*, 2018, **6**, 3869–3875.
35 F. Wang and X. Liu, *J. Am. Chem. Soc.*, 2008, **130**, 5642–5643.
36 J. Zhao, D. Jin, E. P. Schartner, Y. Lu, Y. Liu, A. V. Zvyagin, L. Zhang, J. M. Dawes, P. Xi, J. A. Piper, E. M. Goldys and T. M. Monro, *Nat. Nanotechnol.*, 2013, **8**, 729–734.
37 H. Zhang, Y. Fan, P. Pei, C. Sun, L. Lu and F. Zhang, *Angew. Chem.*, 2019, **131**, 10259–10263.